

**DEVELOPMENT OF CARBON AND POTASSIUM-
INCORPORATED TITANIUM DIOXIDE NANOTUBE
ARRAYS FOR SOLAR ENERGY HARVESTING
APPLICATIONS**

WARAPONG KRENGVIRAT

UNIVERSITI SAINS MALAYSIA

2013

**DEVELOPMENT OF CARBON AND POTASSIUM-INCORPORATED
TITANIUM DIOXIDE NANOTUBE ARRAYS FOR SOLAR ENERGY
HARVESTING APPLICATIONS**

by

WARAPONG KRENGVIRAT

**Thesis submitted in fulfillment of the requirements
for the degree of Doctor of Philosophy**

May 2013

DECLARATION

I hereby declare that I have conducted, completed the research work and written the thesis entitle; *DEVELOPMENT OF CARBON AND POTASSIUM-INCORPORATED TITANIUM DIOXIDE NANOTUBE ARRAYS FOR SOLAR ENERGY HARVESTING APPLICATIONS*. This thesis has not been previously submitted for the degree or diploma in any university, it and does not contain any materials previously published, written or produced by another person.

Signature :
Candidate : Warapong Krengvirat
Date : 1st May 2013

Witnessed by
Signature :
Supervisor : Assoc. Prof. Dr. Srimala Sreekantan
Date : 1st May 2013

ACKNOWLEDGEMENTS

Foremost, I am grateful to acknowledge School of Materials and Mineral Resources Engineering (SMMRE), Universiti Sains Malaysia (USM) for offering an opportunity to pursue my PhD in Materials Engineering: Nanotechnology with sufficient research facilities, great support from administrative, academic and technical staffs. I sincerely appreciate the Japan International Cooperation Agency (JICA) for the financial support and a great opportunity for collaborative research in Matsuda-Muto-Kawamura laboratory, Toyohashi University of Technology (TUT) through AUN/SEED-Net project.

I would also like to express my sincere gratitude to my advisors, Assoc. Prof. Srimala Sreekantan, Prof. Ahmad Fauzi Mohd Noor and Prof. Atsunori Matsuda for the continuous support throughout my doctoral study, for their patience, motivation, enthusiasm, and knowledge. Special thanks go to Assoc. Prof. Srimala Sreekantan for her kind assistance and encouragement. Besides my advisors, I would like to deliver my appreciation to thesis committee for their encouragement, insightful comments, and hard questions.

On top of that, my sincere gratefulness to the Dean of SMMRE, Prof. Hanafi b. Ismail and former Dean, Prof. Ahmad Fauzi Mohd Noor for their concern and invaluable support during my study. Furthermore, I would like to express my appreciation to the Chairs Coordinating Committee of AUN/SEED-Net at SMMRE, Prof. Radzali b. Othman and Prof. Mariatti Jaafar and Prof. Hanafi b. Ismail for consistently support my study in USM.

Last but not least, I would like to take this opportunity to express my heartfelt gratefulness to my beloved parent for unconditional support, motivation and encouragement. I am indebted to my colleagues in USM and TUT for their supports and friendships throughout the years. They have encouraged me toward achieving my research work with wonderful life.

Thank you.

Warapong Krengvirat

May 2013

TABLE OF CONTENTS

	Page
ACKNOWLEDGEMENTS	ii
TABLE OF CONTENTS	iv
LIST OF TABLES	x
LIST OF FIGURES	xii
LIST OF ABBREVIATIONS	xxiii
LIST OF SYMBOLS	xxvi
LIST OF APPENDICES	xxviii
LIST OF PUBLICATIONS	xxix
ABSTRAK	xxxii
ABSTRACT	xxxiii
CHAPTER 1 : INTRODUCTION	1
1.1 Introduction.....	1
1.2 Problem statements.....	4
1.3 Objectives.....	8
1.4 Expected outcome.....	8
1.5 Thesis overview.....	9
CHAPTER 2 : LITERATURE REVIEW	11
2.1 Introduction.....	11
2.2 Solar energy harvesting technologies.....	12
2.2.1 Principle of photoelectrochemical water splitting.....	14

2.2.2	Principle of dye-sensitized solar cell.....	17
2.3	TiO ₂ nanotube arrays.....	19
2.3.1	Anodic growth of self-organized TiO ₂ nanotube arrays.....	20
2.3.2	Factors affecting geometry and composition.....	23
2.3.2.1	Nanotube arrays synthesis using aqueous electrolyte.....	23
2.3.2.2	Nanotube arrays synthesis using organic electrolyte.....	26
2.4	Modification techniques for visible-light harvesting.....	37
2.4.1	Noble metal loading.....	37
2.4.2	Metal ion doping.....	39
2.4.3	Nonmetal doping.....	42
2.4.4	Composite semiconductors and sensitization.....	45
2.5	Crystallization of TiO ₂ nanotube arrays.....	50
2.5.1	Thermal annealing.....	50
2.5.2	Low temperature crystallization by hot water treatment.....	53
2.6	TiO ₂ nanotube arrays as photoanodes.....	56
2.6.1	Photoelectrochemical cells.....	57
2.5.2	Dye-sensitized solar cells.....	59
	CHAPTER 3 : MATERIALS AND METHODOLOGY.....	61
3.1	Introduction.....	61
3.2	Raw materials and chemicals.....	61
3.3	Experimental design.....	63
3.3.1	Formation of visible-light responsive TiO ₂ nanotube arrays.....	64
3.3.2	Low temperature crystallization of TiO ₂ nanotube arrays via hot water treatment	66

3.3.3	Formation of carbon and potassium-incorporated TiO ₂ nanotube arrays.....	67
3.4	Experimental procedure.....	69
3.4.1	Formation of well-aligned TiO ₂ nanotube arrays.....	69
3.4.2	Heat treatment.....	71
3.4.1.1	Thermal annealing.....	72
3.4.1.2	Hot water treatment.....	72
3.5	Characterization.....	73
3.5.1	Electrochemical Impedance spectroscopy.....	73
3.5.1.1	AC impedance analysis.....	74
3.5.1.2	Mott-Schottky analysis.....	75
3.5.2	X-ray diffraction.....	76
3.5.3	Field-emission scanning electron microscopy.....	77
3.5.4	High-resolution transmission electron spectroscopy.....	78
3.5.5	X-ray photoelectron spectroscopy.....	79
3.5.6	Raman spectroscopy.....	80
3.5.7	UV-Vis spectroscopy.....	80
3.5.8	Fourier transform spectroscopy.....	81
3.5.9	Photoluminescence spectroscopy.....	82
3.5.10	Specific surface area measurement.....	83
3.5.11	Photocatalytic activity.....	84
3.5.12	Photoelectrochemical hydrogen generation.....	85
3.5.13	Dye-sensitized solar cells.....	86

CHAPTER 4 : RESULTS AND DISCUSSION.....	89
4.1 Introduction.....	89
4.2 Rapid formation of visible-light responsive TiO ₂ nanotube arrays.....	89
4.2.1 Nanotube formation behavior.....	90
4.2.2 Effect of electrolyte composition on the formation of nanotube arrays	93
4.2.2.1 Effect of water content.....	94
4.2.2.2 Effect of fluoride content.....	100
4.2.3 Effect of applied potential on the formation of nanotube arrays....	107
4.2.3.1 Growth behavior and structural characteristics of nanotube arrays.....	107
4.2.3.2 Phase formation and crystal structure.....	112
4.2.3.3 Chemical state and electronic state.....	117
4.2.3.4 Structural defect state.....	119
4.2.3.5 Light absorption characteristics.....	121
4.2.3.6 Photocatalytic property.....	123
4.2.4 Effect of anodization time on the formation of nanotube arrays....	126
4.2.5 Effect of structural characteristics on the photoelectrochemical hydrogen generation.....	129
4.3 Crystallization of nanotube arrays.....	139
4.3.1 Low temperature crystallization via hot water treatment.....	140
4.3.1.1 Effect of treatment temperature.....	140
4.3.1.2 Effect of treatment condition.....	145
4.3.1.3 Effect of exposure time.....	148
4.3.1.4 Crystallographic structure.....	152

4.3.1.5	Chemical state and electronic state.....	153
4.3.1.6	Structural defect state.....	158
4.3.1.7	Light absorption characteristics.....	160
4.3.1.8	Charge carrier diffusion and recombination.....	161
4.3.1.9	Photocatalytic property.....	163
4.3.2	Structural stability: High temperature crystallization via annealing.....	166
4.3.2.1	Phase formation and crystal structure.....	167
4.3.2.2	Structural characteristics of nanotube arrays.....	171
4.4	Development of carbon and potassium-corporated nanotube arrays.....	173
4.4.1	Formation of carbon and potassium-incorporated TiO ₂ nanotube arrays.....	174
4.4.1.1	Growth behavior and structural characteristics of nanotube arrays.....	175
4.4.1.2	Phase formation and crystal structure.....	182
4.4.1.3	Light absorption characteristics.....	185
4.4.1.4	Photoelectrochemical properties.....	188
4.4.2	Development of dye-sensitized solar cells.....	197
4.4.2.1	Photoelectrochemical properties.....	198
4.4.2.2	Quantum efficiency.....	204
CHAPTER 5 : CONCLUSIONS.....		204
5.1	Conclusions.....	204
5.2	Suggestions for future research work.....	207

REFERENCES..... 208

APPENDICES..... 228

LIST OF TABLES

		Page
Table 2.1	Summary of nanotube length (in μm) obtained by varying the concentration of H_2O of 1 – 3 wt%, and NH_4F of 0.1 – 0.5 wt% in EG with respect to fresh and once-used solution (Prakasam <i>et al.</i> , 2007).	34
Table 2.2	Summary of nanotube inner diameter, outer diameter and length obtained by anodization in fresh-EG containing 2 wt% and 0.3 wt% NH_4F at different applied potential for 17 h (Prakasam <i>et al.</i> , 2007).	36
Table 3.1	Raw materials and chemicals used for the preparation of hybrid TiO_2 nanotube arrays, the fabrication of DSSCs, as well as the photoelectrochemical, photovoltaic and photocatalytic performances evaluation.	62
Table 3.2	The variable and constant parameters for the formation of visible-light responsive TiO_2 nanotube arrays with highly-degree of anatase phase.	66
Table 3.3	The variable and constant parameters for the crystallization of visible-light responsive TiO_2 nanotube arrays via hot water treatment.	67
Table 3.4	The variable and constant parameters for single-step formation of carbon and potassium-incorporated TiO_2 nanotube arrays.	69
Table 4.1	Electrochemical parameters extracted from the complex impedance spectra, and calculated ionic conductivities and the time constants of EG containing 0.5 wt% NH_4F and different contents of H_2O at room temperature.	95
Table 4.2	Structural characteristics of nanotube arrays prepared in EG containing 0.5 wt% NH_4F and different contents of H_2O at 60 V for 1 h.	99
Table 4.3	Electrochemical parameters from the complex impedance spectra, and calculated ionic conductivities and the time constants of EG containing 1 wt% H_2O and different contents of NH_4F at room temperature.	101
Table 4.4	Structural characteristics of nanotube arrays prepared in EG containing 1 wt% H_2O and different contents of NH_4F at 60 V for 1 h.	104

Table 4.5	Structural characteristics of nanotube arrays prepared in EG containing 0.5 wt% NH ₄ F and 1 wt% H ₂ O at different applied potentials for 1 h.	109
Table 4.6	Refinement indexes of the nanotube arrays prepared at different applied potentials after heat treatment at 400°C for 4 h in air.	114
Table 4.7	Structural characteristics of nanotube arrays prepared in EG containing 0.5 wt% NH ₄ F, and 1 wt% H ₂ O at 60 V for different anodization times.	128
Table 4.8	Structural characteristics of nanotube arrays prepared in EG containing 0.5 wt% NH ₄ F, and 1 wt% H ₂ O under different conditions.	130
Table 4.9	V_{fb} and N_d of nanotube arrays with different structural characteristics obtained from MS analysis.	136
Table 4.10	j_p , η and H ₂ evolution rate of photoelectrodes with different structural characteristics.	138
Table 4.11	Refinement indexes of the nanotube arrays after hot water treatment at different temperatures for 3 h.	144
Table 4.12	Refinement indexes of the nanotube arrays after heat treatment at different temperatures for 4 h.	168
Table 4.13	Electrochemical parameters from the complex impedance spectra, and calculated ionic conductivity and the time constants of EG containing 0.5 wt% NH ₄ F and 1 wt% of H ₂ O, and different concentrations of KOH at room temperature.	178
Table 4.14	Structural characteristics of nanotube arrays prepared in EG containing 0.5 wt% of NH ₄ F and 1 wt% of H ₂ O, and different concentrations of KOH.	179
Table 4.15	Structural characteristics of nanotube arrays prepared in EG containing 0.5 wt% NH ₄ F and 1 wt% of 1.0 M KOH at 60 V for different anodization times.	181
Table 4.16	V_{fb} and N_d of nanotube arrays prepared in EG containing 0.5 wt% NH ₄ F and 1 wt% of H ₂ O, and different concentrations of KOH solution.	194
Table 4.17	Structural characteristics of nanotube arrays used in DSSCs.	198
Table 4.18	Photoelectrochemical performance parameters of DSSCs assembled from TiO ₂ nanotube arrays with different structural morphology under simulated solar irradiation.	201

LIST OF FIGURES

		Page
Figure 1.1	Statistic data of global energy consumption and CO ₂ emission during 1990-2011 – plotted from statistic data from British Petroleum, (2012).	1
Figure 1.2	Statistic data of global electricity generation and renewable energy during 1990-2011 – plotted from statistic data from British Petroleum, (2012).	2
Figure 2.1	Main processes in photocatalytic water splitting (Kudo and Miseki, 2008).	12
Figure 2.2	Electronic structures of different metal oxides and relative position of their band edges vs. some important redox potential (Ghicov and Schmuki, 2009).	13
Figure 2.3	Band structures of anatase and rutile TiO ₂ (Leung <i>et al.</i> , 2010).	14
Figure 2.4	Schematic diagram of electrochemical cell. (1) n-type TiO ₂ electrode; (2) Pt counter electrode; (3) ionically conducting separator; (4) gas burette; (5) load resistance; and (6) voltmeter (Hashimoto <i>et al.</i> , 2005).	15
Figure 2.5	Energy diagram of the semiconducting photoanode/liquid electrolyte/metallic cathode system for water photolysis (Radecka <i>et al.</i> , 2008).	16
Figure 2.6	Schematic diagrams of (a) front-side and (b) back-side illumination modes DSSCs using TiO ₂ nanotube arrays.	17
Figure 2.7	Schematic of operation of the DSSC (Gratzel, 2001).	18
Figure 2.8	(a) Oxide formation mechanism on a metal. (b) Morphologies which can be obtained by anodization of Ti metal – a compact oxide film, a disordered nanoporous layer, a self-ordered nanoporous or a self-ordered nanotube layer. (c) Nanotube formation mechanism (Ghicov and Schumuki, 2009).	22
Figure 2.9	Surface morphologies of TiO ₂ nanotube arrays formed in 1 M H ₂ SO ₄ containing 0.1 M HF (pH = 2.8) at (a) 10 V, (b) 15 V, (c) 25 V for 20 h, electrolyte with pH = 3.8 at 10 V for (d) 20 h and (e) 90 h, and (f) electrolyte with pH = 4.5 at 10 V for 20 h (Cai <i>et al.</i> , 2005).	25

Figure 2.10	(a) Cross-sectional, (b) magnified-cross sectional, (c) surface and (d) pore bottom morphologies of TiO ₂ nanotube arrays grown in DMSO containing 2 wt% HF at 60V for 70 h (Ruan <i>et al.</i> , 2005).	28
Figure 2.11	Variation of TiO ₂ nanotube array length as a function of (a) applied voltage for a 70 h anodization using DMSO containing 2% HF with and without a pre-anodization step to template the surface, (b) HF concentration in DMSO for 40 and 60 V 70 h anodization, (c) variation of nanotube length obtained from a 2.0% HF-DMSO containing different deionized water concentrations (40 V, 40 h), and (d) duration for a 40 V anodization in 2.0% HF-DMSO electrolytes with 0%, 3%, and 5% deionized water content (Yoriya <i>et al.</i> , 2007).	29
Figure 2.12	(a) Cross-sectional and (b) surface morphologies of TiO ₂ nanotube arrays grown in FA based at 35 V for 48 h (Shankar <i>et al.</i> , 2007).	31
Figure 2.13	Cross-sectional morphologies of TiO ₂ nanotube arrays prepared in (a) 1 M (NH ₄) ₂ SO ₄ containing 0.5 wt% NH ₄ F, (b) 1:1 of glycerol and water mixture containing 0.5 wt% NH ₄ F, and (c) glycerol containing 0.5 wt% NH ₄ F at 20 V for 3 h. The insets show respective surface morphologies (Macak <i>et al.</i> , 2006).	32
Figure 2.14	(a) – (b) Cross-sectional, (c) bottom and (d) surface morphologies of nanotube arrays grown in EG containing 0.25 wt% NH ₄ F at 60 V for 17 h (Shankar <i>et al.</i> , 2007).	34
Figure 2.15	TiO ₂ loaded with Pt and RuO ₂ , and reaction process of photoelectrochemical water splitting (Leung <i>et al.</i> , 2010).	38
Figure 2.16	Charge transfer from excited TiO ₂ to the different states of metal ions (Leung <i>et al.</i> , 2010).	41
Figure 2.17	(A) VBM XPS spectra of (a) pure TiO ₂ , (b) C-TiO ₂ , (c) S-TiO ₂ , and (d) N-TiO ₂ (Chen and Burda, 2008), and (B) Schematic diagram illustrates the generation of localized state in nonmetal-doped TiO ₂ (Leung <i>et al.</i> , 2010).	44
Figure 2.18	Photocatalytic hydrogen generation with (a) composite semiconductors and (b) metal particle-sensitized TiO ₂ (Leung <i>et al.</i> , 2010).	47
Figure 2.19	X-ray diffraction patterns of TiO ₂ nanotube arrays annealed at temperatures range from 300 to 800°C for 3 h. A, R, and T represent anatase, rutile, and titanium, respectively (Yang <i>et al.</i> , 2008).	51

Figure 2.20	Schematic diagram for the progress of the amorphous–anatase–rutile transformation within the nanotubular walls (cross-section) as a function of O ₂ -annealing temperature at (a) 400, (b) 500, and (c) 600°C. Dotted lines represent degradation of the nanotubular array structure (Hardcastle <i>et al.</i> , 2011).	52
Figure 2.21	Photocurrent transient vs. potential curves of TiO ₂ nanotube layers of a length of 15 μm before and after different treatments in 0.01 M Na ₂ SO ₄ , 10 vol% methanol/DI water solutions using an Ag/AgCl reference electrode under AM 1.5 illumination. Inset: magnification for as-formed and water treated samples (Liu <i>et al.</i> , 2012).	54
Figure 2.22	I–V curves from DSSCs constructed using TiO ₂ nanotube layers of a length of 15 μm before and after different treatments. Inset: magnification for as-formed and water treated samples (Liu <i>et al.</i> , 2012).	55
Figure 2.23	I–V curves from DSSCs constructed using TiO ₂ nanotube layers of a length of 15 μm after water treatment for 0 day, 2 day and 3 day (Lin <i>et al.</i> , 2012).	56
Figure 2.24	j_p transient curves and (B) η curves of nanotube array samples fabricated using a FA containing 0.56 wt% NH ₄ F and 5 wt% H ₂ O at different applied potentials. Prior to photocurrent measurement all samples were annealed at 525°C for 1 h in oxygen (Shankar <i>et al.</i> , 2007).	58
Figure 2.25	(a) comparison of I–V curves of TiO ₂ nanotube arrays-based DSSCs in front-side and back-side illumination modes, and (b) I–V curves of front-side irradiation DSSCs constructed using TiO ₂ nanotube arrays with various lengths (Lei <i>et al.</i> , 2010).	59
Figure 3.1	Flow chart presents an overall methodology for the development of TiO ₂ nanotube arrays for multifunctional applications.	64
Figure 3.2	Flow chart presents the anodic formation of visible-light responsive TiO ₂ nanotube arrays with highly-degree of anatase phase.	65
Figure 3.3	Flow chart presents the crystallization of visible-light responsive TiO ₂ nanotube arrays via hot water treatment.	67
Figure 3.4	Flow chart presents the single-step formation of carbon and potassium-incorporated TiO ₂ nanotube arrays.	68
Figure 3.5	Flow chart presents the anodic formation of TiO ₂ nanotube arrays.	70

Figure 3.6	Illustrates of the connection for potentiostatic anodization using two-electrode configuration.	71
Figure 3.7	Heating profile for thermal annealing of TiO ₂ nanotube arrays.	72
Figure 3.8	Illustration of the experimental setup for hot water treatment.	73
Figure 3.9	Schematic diagrams illustrate (a) polarization in sample cell and simplified equivalent circuit, and (b) cell connection for AC impedance measurement.	74
Figure 3.10	Illustration of three-electrode configuration of Mott-Schottky analysis.	76
Figure 3.11	Illustration of experimental setup for photoelectrochemical hydrogen generation using three-electrode configuration.	85
Figure 3.12	Schematic diagrams illustrate the assembly of back-side illumination DSSCs using TiO ₂ nanotube arrays.	86
Figure 4.1	<i>J-t</i> curve during anodic oxidation of the Ti in EG containing 0.5 wt% NH ₄ F and 1 wt% H ₂ O at 60 V for 1 h. The inset shows the magnified <i>J-t</i> curve in the range of 0 – 3 min.	91
Figure 4.2	FESEM images of oxide layers after anodization in EG containing 0.5 wt% NH ₄ F and 1 wt% H ₂ O at 60 V for (a) 10 and (b) 30 s, and (c) 1 and (d) 3 min. The insets show the cross-sectional of respective morphologies.	91
Figure 4.3	The evolution of nanotube arrays under potentiostatic mode: (a) oxide layer formation, (b) pit formation of the oxide layer, (c) growth of the pit into scallop shaped pores, (d) undissolved metallic portion between the pores undergoes oxidation and field-assisted dissolution, and (e) fully developed nanotube array with a corresponding top view. The magnified image shows the ionic mobility at the oxide/electrolyte interface. –modified from Mor <i>et al.</i> (2006).	93
Figure 4.4	Complex impedance spectra of EG containing 0.5 wt% NH ₄ F, and (a) 0, (b) 1, (c) 2 and (d) 3 wt% H ₂ O.	94
Figure 4.5	FESEM images of nanotube arrays prepared in EG containing 0.5 wt% NH ₄ F, and (a) 0, (b) 1, (c) 2 and (d) 3 wt% H ₂ O at 60 V for 1 h. The insets show the cross-sectional of respective morphologies.	97
Figure 4.6	Idealized geometric relationships in hexagonal nanotubular array with a pore size (<i>D</i>), wall thickness (<i>w</i>), interpore voids distance (<i>v</i>) and interpore distance ($a \approx D + 2w$).	98

Figure 4.7	Complex impedance spectra of EG containing 1 wt% H ₂ O, and (a) 0.1, (b) 0.3, (c) 0.5 and (d) 0.7 wt% NH ₄ F. The inset shows the enlarged spectra at low range of Z' and Z'' .	101
Figure 4.8	FESEM images of oxide layers prepared in EG containing 1 wt% H ₂ O, and (a) 0, (b) 0.1, (c) 0.3, (d) 0.5 and (e) 0.7 wt% NH ₄ F at 60 V for 1 h. The insets show the cross-sectional of respective morphologies	103
Figure 4.9	$J-t$ curves during anodic oxidation of the Ti in EG containing NH ₄ F and H ₂ O with weight ratios of (a) 0.3:2 and (b) 0.5:1 at 60 V for 1 h. The inset shows the magnified $J-t$ curves in the range of 0 – 10 min.	105
Figure 4.10	Comparison between the formation of nanotube arrays and their morphological characteristics under (a) equilibrium, (b) strong oxidation and (c) high dissolution conditions. Red and black arrows represent oxidation and chemical dissolution, respectively.	106
Figure 4.11	$J-t$ curves during anodic oxidation of the Ti in EG containing 0.5 wt% NH ₄ F and 1 wt% H ₂ O at (a) 10, (b) 20, (c) 40 and (d) 60 V for 1 h. The inset shows the magnified $J-t$ curve in the range of 0 – 5 min.	108
Figure 4.12	FESEM images of nanotube arrays prepared in EG containing 1 wt% H ₂ O, and 0.5 wt% NH ₄ F at (a) 10, (b) 20, (c) 40 and (d) 60 V for 1 h. The insets show the cross-sectional of respective morphologies.	109
Figure 4.13	TEM images show (a) surface and (b) cross-sectional morphologies of as-grown nanotube arrays derived from anodic oxidation of the Ti in EG containing 0.5 wt% NH ₄ F and 1 wt% H ₂ O at 60 V for 1 h.	111
Figure 4.14	XRD patterns of (a) as-grown arrays formed at 60 V, and of nanotube arrays prepared at (b) 10, (c) 20, (d) 40 and (e) 60 V for 1 h after heat treatment at 400°C for 4 h in air. The inset shows the magnified patterns of (101) peak.	112
Figure 4.15	(a) TEM and (b) HRTEM images of nanotube arrays formed at 60 V for 1 h after heat treatment at 400°C for 4 h in air. The inset shows the SAED patterns.	115
Figure 4.16	Raman spectra of nanotube arrays prepared at (b) 10, (c) 20, (d) 40 and (e) 60 V for 1 h after heat treatment at 400°C for 4 h in air. The insets show (a) the Raman peak shift in the range from 100 – 250 cm ⁻¹ , and (b) the magnified spectra in the 1100 – 1700 cm ⁻¹ .	116

Figure 4.17	XPS spectra of (a) P25 powder, and (b) nanotube arrays prepared in EG after heat treatment at 400°C for 4 h in air.	117
Figure 4.18	(A) <i>O1s</i> and (B) <i>C1s</i> high resolution XPS spectra of (a) P25 powder and (b) nanotube arrays prepared in EG after heat treatment at 400°C for 4 h in air.	119
Figure 4.19	PL emission spectra of nanotube arrays prepared at (a) 40 and (b) 60 V for 1 h after heat treatment at 400°C for 4 h in air.	120
Figure 4.20	UV-Vis absorption spectra of (a) P25 powder, and (b) nanotube arrays prepared in EG at 60 V for 1 h after heat treatment at 400 °C for 4 h in air.	122
Figure 4.21	Comparison between the bands position of TiO ₂ and C-doped TiO ₂ .	123
Figure 4.22	Visible-light decolorization of MB aqueous solution using (a) blank sample (b) P25 powder and (c) nanotube arrays prepared in EG with subsequent heat treatment at 400 °C for 4 h in air. The inset shows the absorption spectra of residual MB after exposing to nanotube arrays prepared in EG.	124
Figure 4.23	The photocatalytic reactions of carbon-doped TiO ₂ to organic compound. –modified from Peralta-Hernandez <i>et al.</i> (2007).	126
Figure 4.24	FESEM images of nanotube arrays prepared in EG containing 0.5 wt% NH ₄ F, and 1 wt% H ₂ O at 60 V for (a) 15, (b) 30, (c) 45 and (d) 120 min. The insets show the cross-sectional of respective morphologies.	127
Figure 4.25	The nanotube length and growth rate of nanotube arrays prepared in EG containing 0.5 wt% NH ₄ F, and 1 wt% H ₂ O at 60 V for different anodization times.	129
Figure 4.26	<i>j_p</i> curves of sample (a) NT61 under dark conditions, and samples (b) NT11, (c) NT21, (d) NT41, (e) NT45, (f) NT61 and (g) NT62 under simulated solar illumination.	131
Figure 4.27	<i>η</i> curves of sample (a) NT61 under dark conditions, and samples (b) NT11, (c) NT21, (d) NT41, (e) NT45, (f) NT61 and (g) NT62 under simulated solar illumination.	132
Figure 4.28	MS spectra of samples (a) NT11, (b) NT21, (c) NT41, (d) NT45, (e) NT61 and (f) NT62 at 3000 Hz. The inset shows the enlarged spectra in the –0.1 to –0.3 V range.	134
Figure 4.29	<i>j_p</i> transient of samples (a) NT11, (b) NT21, (c) NT41, (d) NT45, (e) NT61, and (f) NT62 under interrupted simulated solar illumination.	137

Figure 4.30	H ₂ evolutions from the samples (a) NT11, (b) NT21, (c) NT41, (d) NT45, (e) NT61, and (f) NT62 under simulated solar illumination.	138
Figure 4.31	FESEM images of (a) as-grown nanotube arrays, and of nanotube arrays after hot water treatment at (b) 50, (c) 60, (d) 70, (e) 80 and (f) 90°C for 3 h.	141
Figure 4.32	The growth of nanocrystals in nanotube arrays by hot water treatment at different temperatures.	142
Figure 4.33	XRD patterns of (a) as-grown arrays, and of nanotube arrays after hot water treatment at (b) 50, (c) 60, (d) 70, (e) 80 and (f) 90°C for 3 h.	143
Figure 4.34	Raman spectra of (a) as-grown arrays, and of nanotube arrays after hot water treatment at (b) 50, (c) 60, (d) 70, (e) 80 and (f) 90°C for 3 h. The insets show the Raman peak shift in the range from 100 – 250 cm ⁻¹ .	145
Figure 4.35	FESEM images of nanotube arrays after (a) dry air treatment and (b) water vapor treatment at 90 °C for 3 h.	146
Figure 4.36	XRD patterns of (a) as-grown arrays, and of nanotube arrays after (b) dry air treatment and (c) water vapor treatment at 90°C for 3 h.	147
Figure 4.37	The formation of anatase structure in TiO ₂ via solid-state mechanism.	147
Figure 4.38	FESEM images of (a) as-grown nanotube arrays, and of nanotube arrays after hot water treatment at 90°C for (b) 1, (c) 3, (d) 6 and (e) 12 h.	149
Figure 4.39	Specific surface areas of nanotube arrays after hot water treatment at 90°C for different exposure times.	150
Figure 4.40	XRD patterns of (a) as-grown arrays, and of nanotube arrays after hot water treatment at 90°C for (b) 1, (c) 3, (d) 6 and (e) 12 h.	151
Figure 4.41	Raman spectra (a) as-grown arrays, and of nanotube arrays after hot water treatment at 90°C for (b) 1, (c) 3, (d) 6 and (e) 12 h. The insets show the Raman peak shift in the range from 100 – 250 cm ⁻¹ .	152
Figure 4.42	(a) TEM image and (b) HRTEM image of nanotube array after hot water treatment at 90°C for 3 h. The inset shows the SAED patterns.	152

Figure 4.43	FTIR spectra of (a) as-grown array, and of nanotube array after hot water treatment at 90°C for (b) 1 and (c) 3 h. The inset shows the magnified spectra in the range 400-800 cm ⁻¹ .	154
Figure 4.44	XPS spectra of (a) as-grown nanotube arrays, and (b) of nanotube arrays after hot water treatment at 90°C for 3 h.	156
Figure 4.45	(A) <i>Cl</i> 1s, (B) <i>Ti</i> 2p, (C) <i>O</i> 1s and (D) <i>F</i> 1s high resolution XPS spectra of (a) as-grown nanotube arrays, and (b) of nanotube array after hot water treatment at 90°C for 3 h.	157
Figure 4.46	PL emission spectra of (a) nanotube arrays after hot water treatment at 90°C for 3 h, and (b) of nanotube arrays annealed at 400°C for 4 h in air.	159
Figure 4.47	UV-Vis absorption spectra of (a) P25 powder, (b) of nanotube arrays after hot water treatment at 90°C for 3 h, and (c) of nanotube array after heat treatment at 400°C for 4 h in air.	160
Figure 4.48	<i>j</i> _p transient of (a) as-grown array, and of nanotube array after hot water treatment at 90 °C for (b) 1, (c) 3, (d) 6 and (e) 12 h under interrupted simulated solar illumination.	162
Figure 4.49	Decolorization of MB aqueous solution using (a) blank sample, (b) as-grown arrays, (c) P25 powder, (d) nanotube arrays after heat treatment at 400°C for 4 h in air, and nanotube array after hot water treatment at 90°C for (e) 1, (f) 3 and (g) 6h.	163
Figure 4.50	Comparison between the photocatalytic reactions of hot water-treated TiO ₂ nanotube arrays and typical TiO ₂ photocatalysts.	165
Figure 4.51	XRD patterns of (a) as-grown arrays, and of nanotube arrays after heat treatment at (b) 200, (c) 300, (d) 400, (e) 500, (f) 600, (g) 700 and (h) 800°C for 4 h.	167
Figure 4.52	Raman spectra of nanotube arrays after heat treatment at (a) 200, (b) 300, (c) 400, (d) 500, (e) 600, (f) 700 and (g) 800°C for 4 h. The insets show the Raman peak shift in the range from 120 – 210 cm ⁻¹ .	170
Figure 4.53	FESEM images of (a) as-grown nanotube arrays, and of nanotube arrays after heat treatment at (b) 200, (c) 300, (d) 400, (e) 500, (f) 600, (g) 700 and (h) 800°C for 4 h. The insets show the cross-sectional of respective morphologies.	172
Figure 4.54	<i>J</i> - <i>t</i> curves during anodic oxidation of the Ti in EG containing 0.5 wt% NH ₄ F and (a) 1 wt% of H ₂ O, and 1 wt % of KOH with (b) 0.5 M (c) 1.0 M and 1.5 M at 60 V for 1 h. The insets show the enlarged <i>J</i> - <i>t</i> curves in the range of 0 – 5 min.	175

Figure 4.55	Complex impedance spectra of EG containing 0.5 wt% NH ₄ F and (a) 1 wt% of H ₂ O, and 1 wt % of KOH with (b) 0.5 M (c) 1.0 M and 1.5 M. The inset shows the enlarged spectra at low range of Z' and Z''.	177
Figure 4.56	FESEM images of the arrays prepared in EG containing 0.5 wt% NH ₄ F and (a) 1 wt% H ₂ O, and 1 wt % of KOH with (b) 0.5 M (c) 1.0 M and 1.5 M. The insets show the cross-sectional of respective morphologies.	179
Figure 4.57	FESEM images of the arrays prepared in EG containing 0.5 wt% of NH ₄ F and (a) 1 wt% of H ₂ O, and 1 wt% of 1.0 M KOH at 60 V for (a) 2 h, (b) 3 h, (c) 5 h and (d) 10 h. The insets show the cross-sectional of respective morphologies.	181
Figure 4.58	Raman spectra of as-grown nanotube arrays prepared in EG containing 0.5 wt% NH ₄ F and (a) 1 wt% of H ₂ O, and 1 wt % of KOH with (b) 0.5 M (c) 1.0 M and (d) 1.5 M. The insets show the Raman peak shift in the range from 100 – 250 cm ⁻¹ .	182
Figure 4.59	Raman spectra of heat-treated nanotube arrays prepared in EG containing 0.5 wt% NH ₄ F and (a) 1 wt% of H ₂ O, and 1 wt % of KOH with (b) 0.5 M (c) 1.0 M and (d) 1.5 M. The insets show the Raman peak shift in the range from 100 – 250 cm ⁻¹ .	184
Figure 4.60	(a) TEM and (B) HRTEM images of heat-treated nanotube arrays prepared in EG containing 0.5 wt% NH ₄ F and 1 wt% of 1.0 M KOH. The inset shows the SAED patterns.	185
Figure 4.61	UV-Vis absorption spectra of (a) P25 powder, and nanotube arrays prepared in EG containing 0.5 wt% NH ₄ F and 1 wt% of (b) H ₂ O, and (c) 1.0 M KOH at 60 V for 1 h after heat treatment at 400°C for 4 h in air.	186
Figure 4.62	XPS spectra of K2p and C1s of the heat-treated arrays prepared in EG containing 0.5 wt% of NH ₄ F and (a) 1 wt% of H ₂ O, and 1 wt % of KOH with (b) 0.5 M (c) 1.0 M and (d) 1.5 M. The inset shows the high resolution XPS spectrum of nanotube arrays prepared in EG containing 0.5 wt% NH ₄ F and 1 wt% of 1.0 M KOH.	187
Figure 4.63	Comparison between the bands position of TiO ₂ , and carbon and potassium-incorporated TiO ₂ .	188

- Figure 4.64 j_p transient curves of (a) heat-treated nanotube arrays prepared in EG containing 1wt% of 1M KOH under dark condition, and of (b) as-grown nanotube arrays obtained from the same condition under illumination as well as of heat-treated nanotube arrays formed in EG containing 0.5 wt% NH_4F and (c) 1 wt% of H_2O , and 1 wt % of KOH solution with (d) 0.5 M (e) 1.0 M and (f) 1.5 M under illumination. 189
- Figure 4.65 η curves of (a) heat-treated nanotube arrays prepared in EG containing 1wt% of 1M KOH under dark condition, and of (b) as-grown nanotube arrays obtained from the same condition under illumination as well as of heat-treated nanotube arrays formed in EG containing 0.5 wt% NH_4F and (c) 1 wt% of H_2O , and 1 wt % of KOH solution with (d) 0.5 M (e) 1.0 M and (f) 1.5 M under illumination. 189
- Figure 4.66 j_p transient curves arise from as-grown nanotube arrays formed in EG containing 0.5 wt% NH_4F and (a) 1 wt% of H_2O , and (b) 1 wt % of 1.0 M KOH under interrupted simulated solar illumination. 190
- Figure 4.67 IPCE curves of heat-treated nanotube arrays prepared in EG containing 0.5 wt% of NH_4F and (a) 1 wt% of H_2O , and (b) 1 wt % of KOH with 1.0 M. The inset shows the enlarged curves in the range of 400 – 800 nm. 192
- Figure 4.68 MS spectra of heat-treated nanotube arrays prepared in EG containing 0.5 wt% NH_4F and (a) 1 wt% of H_2O , and 1 wt % of KOH solution with (b) 0.5 M (c) 1.0 M and (d) 1.5 M. The inset shows the enlarged spectra in the -0.9 to 0 V range. 194
- Figure 4.69 H_2 evolution of nanotube arrays prepared in EG containing 0.5 wt% NH_4F and (a) 1 wt% H_2O , and (b) 1 wt % of 1.0 M KOH. 195
- Figure 4.70 Schematic diagram of back-side illumination DSSCs using TiO_2 nanotube arrays. 197
- Figure 4.71 Photographs of (a) assembled back-side illumination DSSC and (b) the photovoltaic performance evolution of DSSCs under AM 1.5 simulated solar irradiation. 197
- Figure 4.72 $J-V$ curve of NT3h DSSC (a) under dark conditions, (b) under simulated solar illumination and (c) under interrupted simulated solar illumination, and (d) $P-V$ curve under simulated solar illumination. 199
- Figure 4.73 $J-V$ curves of DSSCs as a function of nanotube length (a) under dark conditions, and samples (b) NT15, (c) NT30, (d) NT45, (e) NT60, (f) NT2h, (g) NT3h and (h) NT5h under simulated solar illumination. 200

Figure 4.74 IPCE curves of (a) pristine TiO₂ nanotube arrays, and of (b) 202
NT2h, (c) NT3h and (d) NT5h under simulated solar
illumination.

LIST OF ABBREVIATIONS

AC	Alternating Current
AR	Aspect ratio
BET	Brunauer, Emmet, and Teller theory
C_B	Conduction band
D	Pore size
DC	Direct Current
DEG	Diethylene glycol
DI	Deionized water
DLOS	Deep-level spectroscopy
DMSO	Dimethyl sulfoxide
DSSC	Dye-sensitized solar cell
E_F	Fermi level
EG	Ethylene glycol
EIS	Electrochemical impedance spectroscopy
E_{redox}	Reduction/oxidation potential
E_{counter}	Electrical potential of the working electrode at open circuit conditions
E_{meas}	Electrical potential of the working electrode under illumination
FA	Formamide
FF	Fill Factors
FESEM	Field-emission scanning electron microscopy
FTIR	Fourier transform infrared spectroscopy
FTO	Fluorine-doped tin oxide

G	Geometric surface area factor
GOF	Goodness of fit
HRTEM	High-resolution transmission electron microscopy
ICSD	Inorganic crystal structure database standard
IPCE	Photon to current conversion efficiency
ITO	Tin oxide glass
J	Current density
J_{mp}	Current at maximum power
j_p	Photocurrent density
$J-t$	Current density-time transient
$J-V$	Current density - Voltage
LDA	Local-density approximation
MB	Methylene blue
MEK	Methylethylketone
MO	Methyl orange
MS	Mott-Schottky measurement
N_d	Charge carrier density
NHE	Normal Hydrogen Electrode
NMF	<i>N</i> -methylformamide
P_D	Residual concentration of MB after photodegradation
P_{max}	Maximum power
$P-V$	Power density - Voltage
PEC	Photoelectrochemical water splitting
PEG	polyethylene glycol
PEMFC	Proton exchange membrane fuel cells

PL	Photoluminescence spectroscopy
PTFE	Teflon
R	Resistance
RCA	Radio Corporation of America cleaning method
R_{exp}	Minimum reachable value of R_{wp}
R_p	Diameter of semi-circle of impedance spectrum
R_s	High frequency intersection of impedance spectrum
R_{wp}	Weight residual error
SAED	Selected area electron diffraction
TEG	Triethylene glycol
TEM	Transmission electron microscopy
UV-Vis	UV-Visible spectroscopy
V_B	valence band
VBM	Maximum valence-band
V_{fb}	Flat band potential
V_{mp}	Voltage at maximum power
V_{oc}	Open-circuit voltage
XPS	X-ray photoelectron spectroscopy
XRD	X-ray diffraction
Z	Impedance
Z'	Real impedance
$V_o^{\bullet\bullet}$	Oxygen vacancies

LIST OF SYMBOLS

$h\nu$	Photon energy
ϵ	Dielectric constant of anatase TiO ₂ (48 F m ⁻¹)
ϵ_0	Permittivity of the free space charge (8.86 × 10 ⁻¹² F m ⁻¹)
E_{rev}^0	Reversible potential for water splitting
2θ	Diffraction angle
a	Interpore distance
Å	Angstrom
β	Full-Width at Half-Maximum (radius)
C	Capacitance
C'	Estimated capacitance
e	Electronic charge unit (1.6 × 10 ¹⁹ C)
e^-	Electrons
f	Applied frequency
η	Photoconversion efficiency
h^+	Holes
λ	Wavelength
μ	Growth rate
μ_v	Viscosity
θ	Bragg angle
σ	Ionic conductivity
τ	Crystallite size
τ_{rxn}	Time constant of electrochemical reaction

v	Interpore voids distance
w	Wall thickness
ω_{\max}	Frequency at a maximum imaginary impedance

LIST OF APPENDICES

	Page
APPENDICES	228
Appendix A	229
A1: ICSD data of Anatase TiO ₂ (98-010-5393)	229
A2: ICSD data of Rutile TiO ₂ (98-001-7802)	232
A3: ICSD data of Ti (98-007-1977)	235
Appendix B	238
B1: Abstract of international journal 1: Carbon-incorporated TiO ₂ photoelectrodes prepared via rapid-anodic oxidation for efficient visible-light hydrogen generation, <i>International Journal of Hydrogen Energy</i>	238
B2: Abstract of international journal 2: Low-temperature crystallization of TiO ₂ nanotube arrays via hot water treatment and their photocatalytic properties under visible-light irradiation, <i>Materials Chemistry and Physics</i>	239
B3: Abstract of international journal 3: Single-step growth of carbon and potassium-embedded TiO ₂ nanotube arrays for efficient photoelectrochemical hydrogen generation, <i>Electrochimica Acta</i>	240
B4: Abstract of international journal 4: Photoelectrochemical characterization of WO ₃ -loaded TiO ₂ nanotube arrays via radio frequency sputtering, <i>Electrochimica Acta</i>	241
B5: Abstract of international journal 5: Nanotubular transition metal oxide for hydrogen production, <i>Advanced Materials Research: Nanomaterials</i>	242

LIST OF PUBLICATIONS

International journals

- 1 **Krengvirat W.**, Sreekantan S., Noor A.-F.M., Negishi N., Oh S.Y., Kawamura G., Muto H., Matsuda A. (2012) Carbon-incorporated TiO₂ photoelectrodes prepared via rapid-anodic oxidation for efficient visible-light hydrogen generation, *International Journal of Hydrogen Energy* 37 p.10046–10056.
- 2 **Krengvirat W.**, Sreekantan S., Noor A.-F.M., Negishi N., Kawamura G., Muto H., Matsuda A. (2013) Low-temperature crystallization of TiO₂ nanotube arrays via hot water treatment and their photocatalytic properties under visible-light irradiation, *Materials Chemistry and Physics* 137 p.991–998.
- 3 **Krengvirat W.**, Sreekantan S., Noor A.-F.M., Kawamura G., Muto H., Matsuda A. (2013) Single-step growth of carbon and potassium-embedded TiO₂ nanotube arrays for efficient photoelectrochemical hydrogen generation, *Electrochimica Acta* 89 p.585–593.
- 4 Wei L.C., Sreekantan S., San E.P., **Krengvirat W.** (2012) Photoelectrochemical characterization of WO₃-loaded TiO₂ nanotube arrays via radio frequency sputtering, *Electrochimica Acta* 77 p.128–136.
- 5 Sreekantan S., E P.S., Wei L.C., **Krengvirat W.** (2011) Nanotubular transition metal oxide for hydrogen production, *Advanced Materials Research: Nanomaterials* 364 p.494–499.

Proceedings

- 1 **Krengvirat W.**, Sreekantan S., Noor A.-F.M., Kawamura G., Muto H., Matsuda A. (2012) Low temperature formation of anatase nanocrystals in anodized titania nanotube arrays with hot water treatment, *The 53th Symposium on Glass and Photonics Materials* p.8–9, Japan.
- 2 **Krengvirat W.**, Sreekantan S., Noor A.-F.M., Kawamura G., Muto H., Matsuda A. (2012) Bimetallic transition oxide nanotubes photoelectrode for the production of hydrogen from water, *The 4th International Conference on Applied Energy* p.3221–3226, China.
- 3 **Krengvirat W.**, Sreekantan S., Noor A.-F.M., Kawamura G., Muto H., Matsuda A. (2012) Enhance photoresponse property of titania nanotube arrays by hot-water treatment technique, *The 50th Anniversary Symposium on Basic Science of Ceramics* p.197, Japan.

- 4 **Krengvirat W.**, Sreekantan S., Noor A.-F.M., Matsuda A., Chinwanitcharoen C. (2011) Water content: an essential factor for the preparation of well-aligned TiO₂ nanotubes via anodic oxidation in ethylene glycol electrolyte, *Science and Technology Community Development 2011 & International Symposium on Material Science Engineering and Energy Technology* p.110–119, Thailand.
- 5 **Krengvirat W.**, Sreekantan S., Noor A.-F.M., Matsuda A., Chinwanitcharoen C. (2011) Formation of Self-organized Titanium Oxide by Anodic Oxidation at Different Electrical Potentials and its Photocatalytic Property, *International Conference on Materials Processing Technology 2011* p.27–31, Thailand.
6. Sreekantan S., Lai C.W., E P.S., **Krengvirat W.** (2011) Nanotubular transition metal oxide for hydrogen production, *International Conference of Nanomaterials Synthesis and Characterization 2011*, Malaysia.

Award

- 1 Sreekantan S., Arifin Z.A., Lai C.W., Saharudin K.A. and **Krengvirat W.** (2011) Korea International Women's Invention Exposition 2011, Seoul, Korea, hosted by the Korean Intellectual Property Office (KIPO) and organized by the Korea Women Inventors Association (KWIA) on 4 – 7th May 2011, for project entitle: Nanopurifier- A sustainable way of destroying contaminants in air and water.

PEMBENTUKAN TITANIUM DIOKSIDA TIUBNANO DIGABUNG KARBON DAN KALIUM UNTUK APLIKASI PENGUJAAN SOLAR

ABSTRAK

Tiubnano TiO_2 telah menarik perhatian ramai sebagai bahan yang paling sesuai untuk aplikasi menggunakan tenaga solar. Walaubagaimanapun penyerapan cahaya nampak yang rendah dan rekombinasi cas pembawa yang tinggi masih kekal sebagai isu yang mencabar untuk aplikasi praktikal. Oleh itu, objektif penyelidikan ini adalah untuk membentuk tiubnano TiO_2 untuk aplikasi menggunakan tenaga solar, seperti fotopemerosotan, sel fotoelektrokimia (PEC) dan pewarna-tersensitis sel solar (DSSC). Hasil penyelidikan ini menunjukkan tiubnano TiO_2 yang responsif kepada cahaya nampak telah dibentuk dengan kadar yang pantas $\sim 289 \text{ nm min}^{-1}$ melalui pengoksidaan anodik dalam etilena glikol (EG) yang mengandungi 0.5 wt% ammonium fluorida (NH_4F) dan 1 wt% H_2O . Kehadiran spesies karbonat-terjerap dan karbon pada celahan dalam tiubnano TiO_2 yang berasal daripada pirogenasi EG telah didapati telah didapati menghasilkan jalur setempat di dalam jurang tenaga, lalu mempertingkatkan kebolehan penyerapan cahaya nampak. Tiubnano TiO_2 anatas dengan luas permukaan tinggi ($\sim 110.9 \text{ m}^2 \text{ g}^{-1}$) telah diperolehi setelah merendam tiubnano yang dianodik di dalam air panas pada $\sim 90^\circ\text{C}$. Tiubnano yang dirawat dengan air panas mempamerkan fotopemerosotaan metilena biru yang cekap di bawah cahaya nampak dengan kadar penguraian sebanyak $\sim 11\% \text{ h}^{-1}$; nilai ini lebih tinggi daripada tiubnano yang telah di rawatan haba ($\sim 9\% \text{ h}^{-1}$) dan serbuk P25 ($\sim 2\% \text{ h}^{-1}$). Walau bagaimanapun, rawatan haba pada 400°C selama 4 jam merupakan satu pendekatan penting untuk mendapatkan tahap kehabluran yang baik untuk

mempertingkatkan sifat PEC dan DSSC. Tiubnano TiO₂ yang diberi rawatan haba yang mempunyai panjang purata sebanyak ~18 µm, ketebalan dinding (~13 nm) dan saiz liang yang besar (~115 nm) dengan nisbah aspek yang tinggi (~142.5) mempamerkan keupayaan luar biasa untuk menjana H₂ pada kadar ~508.3 µL min⁻¹ cm⁻² dan kecekapan fotoubahan (η) daripada ~2.3 %. Pertumbuhan tiubnano TiO₂ dan sifat elektrokimianya telah diperbaiki lagi dengan penambahan kalium hidroksida (KOH) ke dalam florin-EG. Gabungan 1 wt% 1.0 M KOH menyebabkan pertumbuhan seimbang tiubnano dengan kadar ~353 nm min⁻¹. Spesies kalium-terjerap meningkatkan lagi penyerapan cahaya nampak kepada ~780 nm. Selain itu, sifat e⁻ daripada kalium-terjerap menggalakkan penambahan pembawa cas (9.7×10^{21} cm⁻³). Tiubnano TiO₂ yang mengandungi karbon dan kalium dengan nisbah aspek ~140.5 menunjukkan sifat fotoelektrokimia yang unggul dan mempunyai kebolehan untuk menjana H₂ dengan kadar evolusi ~658.3 µL min⁻¹ cm⁻² dan η daripada ~2.5 %; iaitu ~30 % lebih tinggi daripada TiO₂ tanpa kalium. Tiubnano TiO₂ yang mempunyai karbon dan kalium digunakan untuk penghasilan DSSCs pencahayaan belakang dengan menggunakan pewarna N719 dan elektrolit iodida/triodideredox. Tiubnano yang tersusun baik dengan panjang purata sebanyak 18 µm, tebal dinding (~13 nm), dan saiz liang~130 nm didapati membenarkan penembusan $h\nu$ teruja yang lebih banyak dan memudahkan resapan pembawa cas. Tambahan pula, luas permukaan geometri yang tinggi sebanyak ~755 dapat mengujakan penyerapan pewarna yang tinggi. η maksimum sebanyak 2.78 % telah dicapai daripada tiubnano TiO₂ yang mempunyai panjang purata sebanyak 17.8 µm dengan potensi litar terbuka sebanyak 0.67 V, ketumpatan arus 8.95 mA cm⁻², dan faktor terisi 46.39 %.

**DEVELOPMENT OF CARBON AND POTASSIUM-INCORPORATED
TITANIUM DIOXIDE NANOTUBE ARRAYS FOR
SOLAR HARVESTING APPLICATIONS**

ABSTRACT

TiO₂ nanotube arrays have attracted great interest as the most promising candidate for solar energy harvesting applications. However, poor visible-light absorption and high recombination of charge carriers still remain as challenging issues for their practical applications. Hence, the objective of this work was to develop carbon and potassium-incorporated TiO₂ nanotube arrays for solar energy harvesting applications, including photodecolorization, photoelectrochemical cell (PEC) and dye-sensitized solar cells (DSSC). Visible-light responsive TiO₂ nanotube arrays were rapidly grown with a rate of ~289 nm min⁻¹ by anodic oxidation in ethylene glycol (EG) containing 0.5 wt% ammonium fluoride (NH₄F) and 1 wt% H₂O. The presence of adsorbed-carbonate species and interstitial carbon in TiO₂ nanotubes originated from the pyrogenation of EG resulted in the generation of localized state, and thus enabled the visible-light absorption. Anatase TiO₂ nanotube arrays with high surface area (~110.9 m² g⁻¹) were obtained by facile immersion of as-anodized nanotube arrays in hot water at ~90°C. Such hot water-treated nanotube arrays exhibited efficient visible-light photodegradation of methylene blue with the decomposition rate of ~11 % h⁻¹. This value is relatively higher than heat-treated arrays (~9 % h⁻¹) and P25 powder (~2 % h⁻¹). However, heat treatment at 400°C for 4 h was found as essential approach to obtain better crystallinity for high PEC and DSSC properties. Heat-treated TiO₂ nanotube arrays with average nanotube lengths

of $\sim 18 \mu\text{m}$, thick walls ($\sim 13 \text{ nm}$) and large pore sizes ($\sim 115 \text{ nm}$), with high aspect ratio (~ 123.6) exhibited remarkable ability to generate H_2 at a rate of $\sim 508.3 \mu\text{L min}^{-1} \text{ cm}^{-2}$ and photoconversion efficiency (η) of $\sim 2.3\%$. The growth of TiO_2 nanotube arrays and their electrochemical properties were further improved by simple addition of potassium hydroxide (KOH) into fluorinated-EG. The incorporation of 1 wt% of 1.0 M KOH facilitated an equilibrium growth of nanotube arrays with a rate of $\sim 353 \text{ nm min}^{-1}$. The adsorbed-potassium species further extended the light visible-light absorption to $\sim 780 \text{ nm}$. Furthermore, the electron donation nature of adsorbed-potassium promoted larger number of charge carriers ($9.7 \times 10^{21} \text{ cm}^{-3}$). Carbon and potassium-incorporated TiO_2 nanotube arrays with aspect ratio of ~ 140.5 exhibited superior photoelectrochemical H_2 generation with an evolution rate of $\sim 658.3 \mu\text{L min}^{-1} \text{ cm}^{-2}$ and η of $\sim 2.5\%$, which is $\sim 30\%$ higher than that of without potassium. Carbon and potassium-incorporated TiO_2 nanotube arrays were assembled to back-side illumination DSSCs using N719 dye and iodide/triiodide redox electrolyte. Well-aligned nanotubes with average nanotube lengths of $18 \mu\text{m}$, thick walls ($\sim 13 \text{ nm}$), and large pore sizes ($\sim 130 \text{ nm}$) allowed a greater penetration of excited $h\nu$ and ease charge carrier diffusion. Furthermore, high geometric surface area up to ~ 755 could harvest higher dye adsorption. A maximum η of 2.78% was achieved from a $17.8 \mu\text{m}$ length TiO_2 nanotube arrays, with open circuit potential of 0.67V , current density of 8.95 mA cm^{-2} , and filled factor of 46.39% .

CHAPTER 1

INTRODUCTION

1.1 Introduction

Global warming is an important issue faced by humankind, which causes an unprecedented onslaught of deadly and costly weather disasters, such as severe storms, droughts, heat waves, rising seas and floods throughout the world. The combustion of fossil fuel from human activities, such as transportation and industry massively increase the energy consumption thus contributes to global warming by releasing billion tons of greenhouse gases, such as carbon dioxide (CO₂), methane (CH₄), nitrous oxide (N₂O) and fluorinated gases into atmosphere. Figure 1.1 shows statistic data of fossil fuel consumption and CO₂ emission reported by British Petroleum public limited company; BP (British Petroleum, 2012). The fossil fuel consumption increases continuously year by year and the overall consumptions are estimated approximately eight times higher than alternative sources, for example nuclear- and hydro-energy.

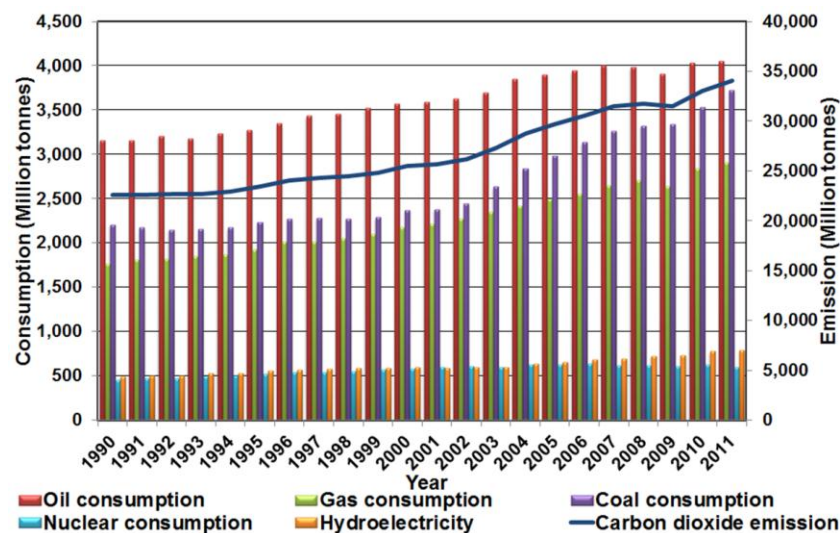


Figure 1.1 Statistic data of global energy consumption and CO₂ emission during 1990-2011 – plotted from statistic data from British Petroleum, (2012).

High consumption of fossil fuel also leads to energy crisis which strongly impacts the economic globalization by arising the energy price. Besides, the emissions of effluents gaseous or wasted water from human activities contribute to the deleterious effects on an environment and the earth ecosystems (Akpan *et al.*, 2009). Pursuant to aforementioned issues, it is indispensable to explore sustainable solutions to safe the earth and mankind. Over the last decades, abundant resources, including geothermal, solar and wind have drawn considerable attention as alternative resources for inexhaustible and non-polluting “GREEN” energy. However, they can subsidies approximately 15% of overall electricity generation (Figure 1.2).

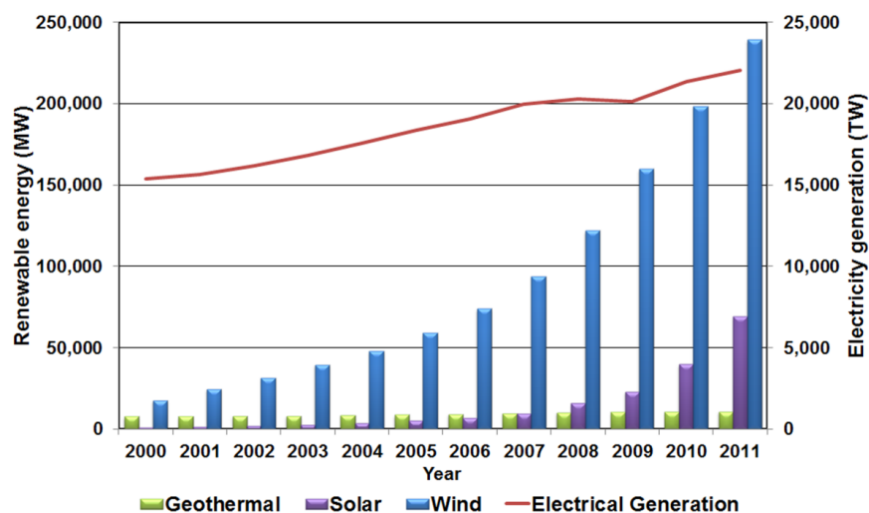


Figure 1.2 Statistic data of global electricity generation and renewable energy during 1990-2011 – plotted from statistic data from British Petroleum, (2012).

Solar energy; radiant light and heat from the sun, is the most abundant clean energy source available. Despite the fact that solar energy strikes the earth in an hour is relatively higher than energy consumed by humans for an entire year (Lewis, 2007). Hence, extensive research and development of materials that can efficiently harvest solar irradiation and convert it to clean and renewable energy are essential. Photocatalysis which utilizes solar energy to activate the chemical reactions via

oxidation and reduction is a sustainable technology to provide solution for energy crisis and environmental issues (Kudo and Miseki, 2008; Vinu and Madras, 2010). Photoelectrochemical water splitting; PEC (Fujishima and Honda, 1972) and dye-sensitized solar cell; DSSC (O'regan and Gratzel, 1991) appear as potential means to convert solar energy to hydrogen (H₂) fuel and electricity, respectively. Several types of photocatalyst, such as TiO₂, ZnO, Fe₂O₃, ZrO₂, V₂O₅, Nb₂O₅ and WO₃ have been used in PECs and DSSCs. Among them, TiO₂ is one of the most promising candidates because of its superior properties, *e.g.*, light absorption capabilities, chemical inertness and stability (Ni *et al.*, 2007; Chen *et al.*, 2007; Varghese *et al.*, 2009). It possesses suitable band-edge positions that enable its use in PECs and DSSCs. Furthermore, its strong oxidation nature offers a great ability in detoxifying hazardous waste and air contaminant (Fujishima and Honda, 1972).

One-dimension (1D) nanostructured material has been discovered (Iijima, 1991), and it has been triggered enormous effort in physics, chemistry, and materials science. TiO₂ with well-aligned nanotubular structure provides unique electronic properties, such as high *e*⁻ mobility, low quantum confinement effects, high specific surface area, excellent ability to harvest photon energy (*hν*), and high mechanical strength (Mohapatra *et al.*, 2007; Baker and Kamat, 2009; Roy *et al.*, 2011). Furthermore, vectorial charge transport facilitates the photoelectrochemical properties and photocatalytic efficiency (Baker and Kamat, 2009; Mohamed and Rohani, 2011). These advantages render TiO₂ nanotube arrays as a promising candidate for various applications, such as for pollutant detoxification (Chen *et al.*, 2009; Sreekantan *et al.*, 2010; Sangpour *et al.*, 2010), PECs (Park *et al.*, 2006; Mohapatra *et al.*, 2007; Palmas *et al.*, 2010) and DSSCs (Jennings *et al.*, 2008; Lei *et*

al., 2010; Premalal *et al.*, 2012; Chang *et al.*, 2012). Although a promising structure of TiO₂ has been established, poor visible-light absorption of wide bandgap semiconductor (*c.a.* 3.2 eV) and high recombination of charge carriers restrict its use under solar irradiation. Therefore, this research established an efficient approach to form carbon-incorporated TiO₂ nanotube arrays via anodic oxidation in ethylene glycol (EG) containing excessive fluoride ions (F⁻) for solar harvesting applications.

The growth of TiO₂ nanotube arrays was further improved by incorporation of alkali-species through the addition of potassium hydroxide (KOH) into EG. This approach allowed the simultaneous control of electrochemical oxidation and chemical dissolution, thereby enhancing the growth rate and structural morphologies of nanotube arrays. Adsorbed-potassium species on TiO₂ nanotubes contributed to their visible-light absorption and photoelectrochemical properties. This research also demonstrated an alternative method to crystallize TiO₂ nanotube arrays at low-temperature via water treatment. In addition, the crystallization behavior and structural stability of nanotube arrays was also determined by thermal annealing at high temperature. The photoelectrochemical water splitting and photodegradation under solar irradiation were carried out in custom made reactors. Furthermore, back-side illumination DSSCs were fabricated in order to further determine the performance of nanotube arrays to harvest the solar energy.

1.2 Problem statements

Since scientific studies of TiO₂ has been established in the early of 20th century (Keidel, 1929), TiO₂ has become one of the most widely used materials due to its unique physio-chemical properties (Hashimoto *et al.*, 2005). However, their

poor visible-light absorption and high recombination of charge carriers restrict their use under solar irradiation (Sennik *et al.*, 2010; Sreekantan *et al.*, 2010). The recombination of photogenerated charge carrier due the diffusion length of $\sim 10 - 30$ nm (Lei *et al.*, 2010) can be overcome by the use of nanotubular structure. Recently, synthesis of TiO₂ nanotube arrays by anodic oxidation has been attracting considerable interest to aforementioned purposes. Effects of various synthesis parameters, *e.g.*, electrical potential (Gong *et al.*, 2001; Paulose *et al.*, 2007), anodization time (Wan *et al.*, 2009; Palmas *et al.*, 2010), electrolyte type and chemical composition (Shankar *et al.*, 2007; Hu *et al.*, 2008) have been extensively investigated.

The anodic oxidation in EG has been suggested as an efficient method to form well-aligned TiO₂ nanotube arrays with ultra-high aspect ratios (Paulose *et al.*, 2006; Shankar *et al.*, 2007). Furthermore, it is the only process that allows the incorporation of carbon species into nanotubes without any additional processing (Hu *et al.*, 2007; Park *et al.*, 2006; Raja *et al.*, 2007). The adsorbed-carbon species from EG induce the generation of a localized C2*p* state above O2*p* states, thereby enabling the visible-light absorption (Mohapatra *et al.*, 2007; Liu *et al.*, 2009). Numerous researchers have achieved the formation of ultra-long TiO₂ nanotube arrays up to 1000 μm (Paulose *et al.*, 2007; Shankar *et al.*, 2007; Prakasam *et al.*, 2007). In these reported works, the formation of long nanotube arrays however requires long production time of $\sim 17 - 216$ h. Such conditions suppress the utilization of anodic oxidation to be applied in the industrial scales and thus hinder the usage of TiO₂ nanotube arrays. From these aspects, the development of an

anodization process for the rapid formation of TiO₂ nanotube arrays turns into an attractive subject of this study.

The anodic-growth of TiO₂ nanotube arrays is well-known as the equilibrium reaction between electrochemical oxidation and chemical dissolution (Sreekantan *et al.*, 2010; Sennik *et al.*, 2010). The growth of long nanotubes is significantly hindered by high chemical dissolution at the top of nanotubes (Macak *et al.*, 2006; Shankar *et al.*, 2007). Wang *et al.* (2011) have recently proposed the solution to control the chemical dissolution in EG containing ammonium fluoride (NH₄F) electrolyte by addition of sodium carbonate (NaCO₃) which allowed the formation of nanotube arrays with fast growth rate. This implies the potential of alkali additives to improve the balance between electrochemical oxidation and chemical dissolution. Besides, the incorporation of alkali species into TiO₂ nanotube arrays contributed to better photoelectrochemical properties as demonstrated by the anodic growth of TiO₂ nanotube arrays in hydrofluoric acid electrolyte containing potassium salt (Richter *et al.*, 2009). Although high growth rate has been achieved, the photoelectrochemical properties of nanotube arrays obtained from EG containing alkali species remains to be determined. Hence, this research devotes to develop carbon and potassium-incorporated TiO₂ nanotube arrays with enhanced electrochemical properties by rapid-anodic oxidation in fluorinated-EG containing alkali species.

Besides, heat treatment process has also drawn an essential role in determining the crystal structure of TiO₂ nanotube arrays. High annealing temperature to form high crystallinity anatase phase (*c.a.* 280 – 600°C) induces the formation of thick barrier layer and thus lowers the photocatalytic efficiency of TiO₂

nanotube arrays by the recombination of charge carriers. Therefore, the investigation of crystallization behavior and structural stability of TiO₂ nanotube arrays at different heat treatment temperature are crucial to define their morphology and crystallinity, as well as the integration of this nanostructure into the devices. The development of low temperature crystallization of TiO₂ nanotube arrays is essential to the integration of TiO₂ nanotube arrays with polymeric substrates or temperature-sensitive devices. Alternatively, Matsuda *et al.* (2000) have suggested a facile approach to crystallize titanate-based thin films by immersion of the oxide into hot water. The products showed superior characteristics, *e.g.*, wettability, optical properties, photocatalytic efficiency and photovoltaic performance. Therefore, the mechanistic study for the crystallization of carbon-incorporated TiO₂ nanotube arrays by hot water treatment is essential to be explored as an alternative to thermal annealing.

TiO₂ nanotube arrays have widely been used in photoelectrochemical and photocatalytic applications. However, the understanding in the influence of structural characteristics of nanotube arrays on their efficiency remains unclear. For example, Park *et al.* (2006) suggested that the photoelectrochemical efficiency of nanotube arrays is proportional to the nanotube length. Liu *et al.* (2009) later demonstrated that the pore diameter has a greater effect rather than the nanotube length. It is of interest to study the influence of structural characteristics of TiO₂ nanotube arrays for solar energy harvesting applications. The role of carbon and potassium species in nanotubes on the visible-light response and their properties is also essential to address. Hence, comprehensive studies need to be conducted to obtain mechanistic model on how the carbon and potassium species improve the visible-light absorption, as well as photocatalytic and photoelectrochemical efficiency. Therefore, it is of

interest to gain fundamental knowledge on the fabrication of PEC and DSSC devices using carbon and potassium-incorporated TiO₂ nanotube arrays as photoelectrodes.

1.3 Objectives

The objectives of this research work are described as follows;

1. To study rapid formation of carbon incorporated TiO₂ nanotube arrays by anodization method in EG.
2. To improve the growth and properties of carbon incorporated TiO₂ nanotube arrays with KOH addition in EG.
3. To study the crystallization of TiO₂ nanotube arrays via hot water treatment and thermal treatment.
4. To investigate the photocatalytic and photoelectrochemical properties of visible-light responsive TiO₂ nanotube arrays.

1.4 Expected outcome

The ultimate outcomes of this research work are detailed as follows;

- Fundamental knowledge on the formation visible-light responsive TiO₂ nanotube arrays for solar energy harvesting applications is the main outcomes of this research work.
- With the fundamental knowledge of the formation gathered from this research work, a mechanistic model on the growth of TiO₂ nanotube arrays is proposed which is essential for the control of structural morphologies of TiO₂ nanotube arrays by controlling the anodic oxidation parameters.
- Data on the electrochemical, chemical, structural, electronic, morphological and optical properties, as well as photocatalytic and photoelectrochemical properties

would contribute towards the knowledge of microstructure-properties relation of photocatalysts in nanoscale.

- Eventually, by acquiring this important fundamental knowledge on the formation of visible-light responsive TiO₂ nanotube arrays and their usage in PECs and DSSCs, the project is believed to benefit the Universities as well as the countries in the development of high efficiency PECs and DSSCs.

1.5 Thesis overview

This thesis is organized in five chapters consequently. Chapter 1 describes a brief introduction, problem statements, objectives and outcomes of the research. In chapter 2, a comprehensive review on the formation of TiO₂ nanotube arrays and fundamental concepts of photocatalysis and functional applications of TiO₂ nanotube arrays, including photoelectrochemical water splitting and dye-sensitized solar cells are elaborated. This includes a comprehensive review on the enhancement of photocatalytic efficiency by the incorporation of noble loading, metal ion and anion doping, composite semiconductors and sensitization. Chapter 3 details the experiment procedures that were used in this study. This included the experimental design and the preparation of TiO₂ nanotube arrays with the incorporation of carbon and potassium species. The characterization techniques are described in detail. This covers a brief explanation on the characterization equipment, their operation principles and sample preparation.

Chapter 4 presents the experimental results and comprehensive discussion on the formation of TiO₂ nanotube arrays via rapid-anodic oxidation and their applications under solar light irradiation. The content consists of main three parts,

including 1) the detail investigation on the growth behavior of visible-light responsive TiO₂ nanotube arrays by varying anodic oxidation parameters (*e.g.*, electrolyte composition, applied potential and anodization time) and effect of structural characteristics on their photoelectrochemical properties, 2) the crystallization of nanotube arrays via hot water treatment at different temperatures and exposure times, and the thermal stability of nanotube arrays at different temperatures, and 3) the formation of carbon and potassium-incorporated TiO₂ nanotube arrays by incorporation of KOH solution into fluorinated-EG electrolyte. The potential for newly-developed TiO₂ nanotube arrays for solar energy harvesting applications, such as photoelectrochemical water splitting and photodegradation under solar irradiation, as well as dye-sensitized solar cell are discussed in detail. Finally, chapter 5 is devoted to the conclusions of this research work and suggestions for future work.

CHAPTER 2

LITERATURE REVIEW

2.1 Introduction

TiO₂ nanotube arrays have attracted scientific interest due to the combination of functional material properties with controllable nanostructure. Superior properties of TiO₂ nanotube arrays, including vectorial pathway of e^- transport, minimized e^- recombination, and high specific surface area render them as the most promising candidate for solar energy harvesting applications. Photoelectrochemical cells (PECs) and dye-sensitized solar cells (DSSCs) assembled with TiO₂ nanotube arrays have attracted great interest due to their outstanding potential to convert solar energy to hydrogen (H₂) fuel and electricity, respectively. However, the performance of PECs and DSSCs are greatly determined by structural morphologies of nanotube arrays. Hence, related literatures on the development of TiO₂ nanotube arrays for solar harvesting applications are elaborated in this chapter.

This chapter provides comprehensive review on the following topics: 1) basic principle of photocatalyst, PECs and DSSCs, 2) formation mechanism of oxide via anodization, and effects of anodization parameters to the formation of TiO₂ nanotube arrays, 3) electronic structure modification strategies, *e.g.*, noble metal loading, metal doping, nonmetal doping, semiconductor composite and sensitization for efficient solar harvesting applications, 4) the crystallization of TiO₂ nanotube arrays, and 5) the significance of structural morphologies of nanotube arrays on the performance of PECs and DSSCs.

2.2 Solar energy harvesting technologies

Innovations in materials science related to photoelectrochemical technology play a key role in the paradigm shift from fossil fuel to clean and renewable sources (Varghese *et al.*, 2009). PECs (Fujishima and Honda, 1972) and DSSCs (O'regan and Gratzel, 1991) have been recognized as potential technologies to aforementioned transition by generating clean and renewable energy from solar energy. Photoelectrochemical solar energy conversion devices involve photosensitizers that absorb light and engage in electron-transfer reaction (Kalyanasundaram and Gratzel, 1998). Figure 2.1 illustrates the main steps involved in photocatalytic water splitting process under illumination.

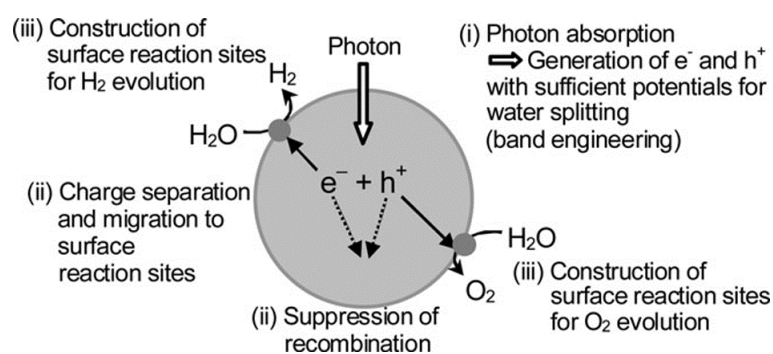


Figure 2.1 Main processes in photocatalytic water splitting (Kudo and Miseki, 2008).

Numerous n-type semiconductors, such as TiO₂, ZnO, Fe₂O₃, ZrO₂, V₂O₅, Nb₂O₅ and WO₃ have been integrated for PECs and DSSCs as photoanodes (Kalyanasundaram and Gratzel, 1998; Chicov and Schmuki, 2009). However, relative positions of band edges play a key role in determining their chemical applications. For PEC, the bottom level of conduction band (C_B) edge needs to be more negative than the redox potential of H⁺/H₂ (0 V *vs.* normal hydrogen electrode: NHE), while the top level of the valence band (V_B) be more positive than the redox potential of H₂O/O₂ (*c.a.*, 1.23

eV) –refer to Figure 2.2. Therefore, the theoretical minimum band gap energy for water splitting is 1.23 eV that corresponds to the wavelength (λ) of light at approximately 1,100 nm (Kudo and Miseki, 2008; Ghicov and Schmuki, 2009).

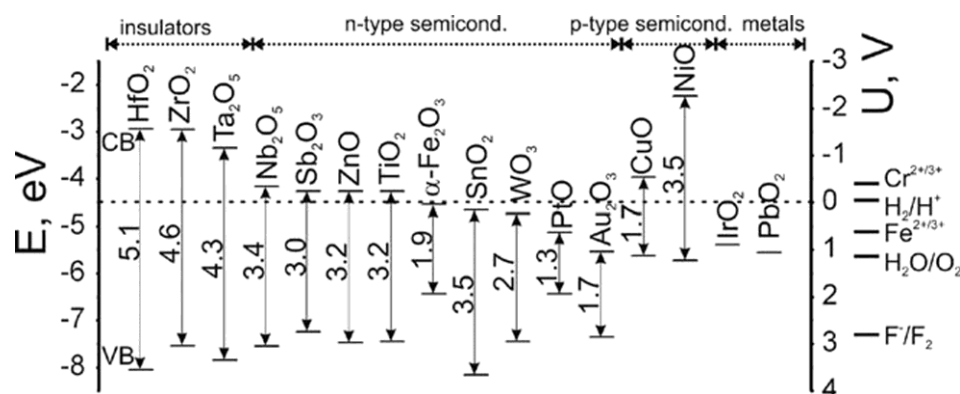


Figure 2.2 Electronic structures of different metal oxides and relative position of their band edges vs. some important redox potential (Ghicov and Schmuki, 2009).

Among qualified candidates, TiO₂ is the most promising candidate to be used as photoelectrode because of its superior properties, for example strong oxidation, high stability and against photocorrosion (Chen *et al.*, 2007; Varghese *et al.*, 2009; Lei *et al.*, 2010). TiO₂ exists in three different structures (anatase, rutile and brookite), the anatase and rutile phases have been widely used for solar energy harvesting applications (Mohapatra *et al.*, 2007; Kang *et al.*, 2009; Premalal *et al.*, 2012). The band gap energies of anatase and rutile are 3.2 and 3.0 eV, corresponding to absorption thresholds at 390 and 415 nm, respectively (Rao *et al.*, 1980). This infers that rutile phase can absorb a more extensive range of light. The V_B positions of these two phases is almost the same (*c.a.* 3.0 V), but the C_B positions are slightly different (Figure 2.3). The C_B potential of rutile is slightly different from the NHE potential, whereas anatase is shifted cathodically by 0.2 V. This indicates relatively high

driving force of anatase phase for the reduction of water as compared to rutile phase (Lueng *et al.*, 2010).

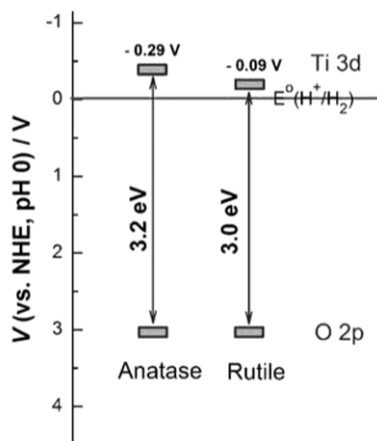


Figure 2.3 Band structures of anatase and rutile TiO₂ (Lueng *et al.*, 2010).

Remarkable advantages of anatase TiO₂ render them as efficient photoanode in DSSCs (O’regan and Gratzel, 1991; Jennings *et al.*, 2008; Lei *et al.*, 2010; Wang *et al.*, 2010). However, the photoconversion efficiency of DSSCs is strongly dependent on the dye semiconductor and a redox mediator (Kalyanasundaram and Gratzel, 1998; Adachi *et al.*, 2007). Therefore, it is dispensable to understand the operation principle of PEC and DSSC in order to utilize TiO₂ nanotube arrays as efficient photoanode for solar energy harvesting applications.

2.2.1 Principle of photoelectrochemical water splitting

Hydrogen is an ideal, renewable and clean energy carrier and one of the most promising alternates for the fossil fuel in the future. The utilization photocatalyst for solar energy harvesting using PEC is essential for sustainable H₂ production (Zhang *et al.*, 2010; Gong *et al.*, 2010). The PEC system consists of a semiconductor working electrode (*i.e.* nanocrystalline TiO₂ film) and platinum (Pt) counter

electrode, both immersed in an aqueous electrolyte (Fujishima and Honda, 1972) as illustrated in Figure 2.4.

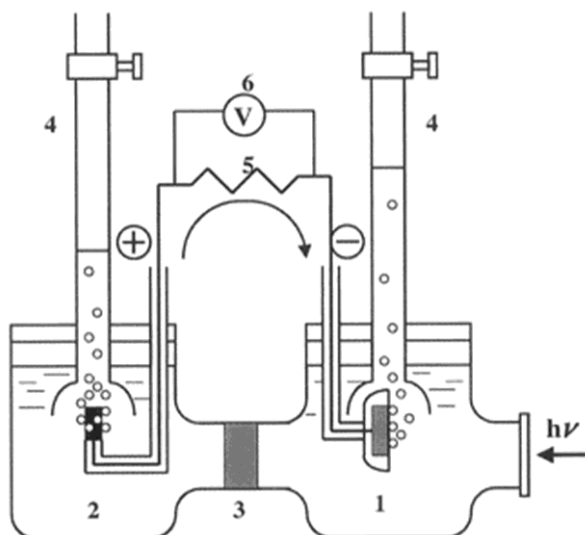
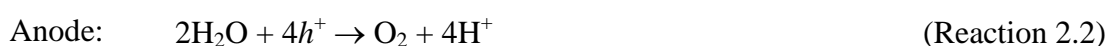


Figure 2.4 Schematic diagram of electrochemical cell. (1) n-type TiO₂ electrode; (2) Pt counter electrode; (3) ionically conducting separator; (4) gas burette; (5) load resistance; and (6) voltmeter (Hashimoto *et al.*, 2005).

Upon illumination with sufficient light energy ($h\nu$), electrons (e^-) in the V_B are excited into the C_B , creating an electron-hole pairs in the semiconductor. The e^- are transported from the C_B via an external wire to the Pt cathode where the H₂ evolution reaction occurs through the reduction of water (H₂O). On the other hand, the holes (h^+) are transported to the photoanode surface where they oxidize H₂O to produce oxygen gas (O₂). By this means, H₂ and O₂ are produced at different electrodes, and can be collected in separate storage volumes. The electrochemical reactions at the cathode and photoanode are:





In addition, the flat band potential (V_{fb}) at the photoanode/electrolyte interface is also essential to determine the efficiency of PEC. The band bending at the photoanode/electrolyte interface is a result of solid-electrolyte interface phenomena (Figure 2.5). The Fermi level (E_F) in a semiconductor and electrochemical reactions in the electrolyte (E_{redox}) are equal at the equilibrium state. The space charge region is formed at the interface. This space charge region provides a strong electric field that is indispensable for an effective separation of photoexcited e^- from h^+ . On the other hand, if light is absorbed in the bulk of the photoanode, the photoexcited e^- and h^+ are created, but there is a high possibility for recombination to occur during water photolysis (Redeka *et al.*, 2008).

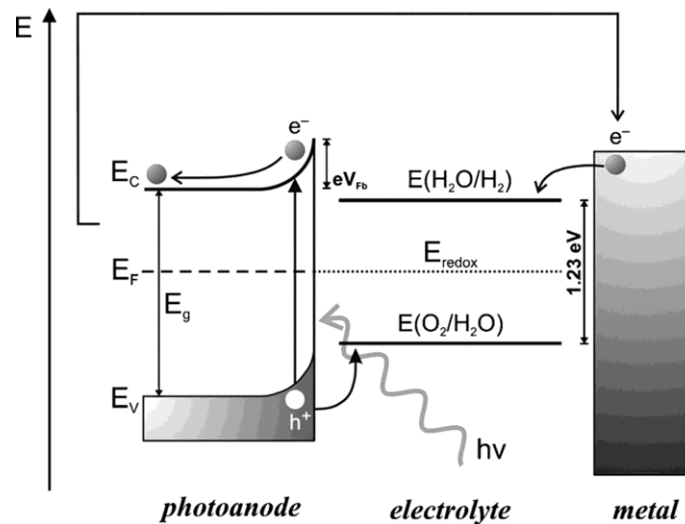


Figure 2.5 Energy diagram of the semiconducting photoanode/liquid electrolyte/metallic cathode system for water photolysis (Radecka *et al.*, 2008).

2.2.2 Principle of dye-sensitized solar cell

Dye-sensitized solar cell has been recognized as a viable competitor to the well-developed silicon solar cell which is relatively expensive (Varghese *et al.*, 2009; Lei *et al.*, 2010). A typical DSSC is assembled with a nanocrystalline TiO₂ film on fluorine-doped tin oxide (FTO) glass which is covered with a monolayer of dye molecules, redox mediator, and Pt-coated FTO glass (O'regan and Gratzel, 1991; Wang and Lin, 2010). Several types of ruthenium bipyridyl dyes (*i.e.*, black dye, N3 and N719) are often used as the dye, while iodide/tri-iodide (I⁻/I₃⁻) redox electrolyte is used as the redox mediator (Adachi *et al.*, 2007; Lei *et al.*, 2010; Zhang *et al.*, 2011). Considerable efforts have been devoted to develop TiO₂ nanotube arrays on FTO glass and use as photoanode (TiO₂/FTO) for front-side illumination –refer to Figure 2.6a (Varghese *et al.*, 2009; Lei *et al.*, 2010). However, the fabrication of TiO₂/FTO involves the sputtering of Ti-films on FTO glass, thus leading to high fabrication cost (Lei *et al.*, 2010).

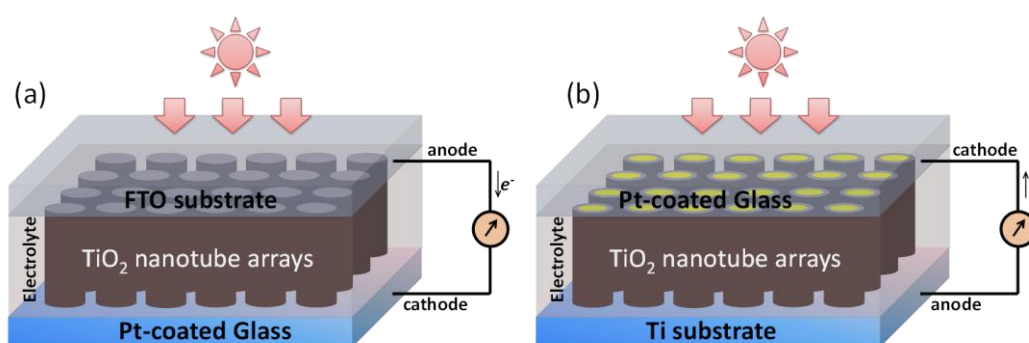


Figure 2.6 Schematic diagrams of (a) front-side and (b) back-side illumination modes DSSCs using TiO₂ nanotube arrays.

TiO₂ nanotube arrays on Ti substrate (TiO₂/Ti) have later been developed to overcome aforementioned problem (Kuang *et al.*, 2008). TiO₂/Ti-based DSSCs require back-side illumination (Figure 2.6b), which limits the enhancement of

photoelectrochemical performance because the platinized-counter electrode partially reflects light, and also induce high resistance at the metal/oxide interface (Varghese *et al.*, 2009; Wang and Lin, 2010). Figure 2.7 illustrates the reaction in DSSC under illumination. Optical excitation of the dye with $h\nu$ leads to the transition of e^- in the dye from equilibrium state to an excited state (Reaction 2.5). Photoexcited e^- rapidly moves from dye into the C_B of TiO_2 , thereby remaining a positively charged state (Reaction 2.6). The dye accepts e^- , then regenerate I_3^- from $3I^-$ in the electrolyte (Reaction 2.7). The I_3^- formed in the dye regeneration process diffuse through the liquid phase to the cathode, where they are reduced back to $3I^-$ to complete the cycle by receiving an e^- from redox mediator –refer to Reaction 2.8 (Kalyanasundaram and Gratzel, 1998; Adachi *et al.*, 2007; Jennings *et al.*, 2008).

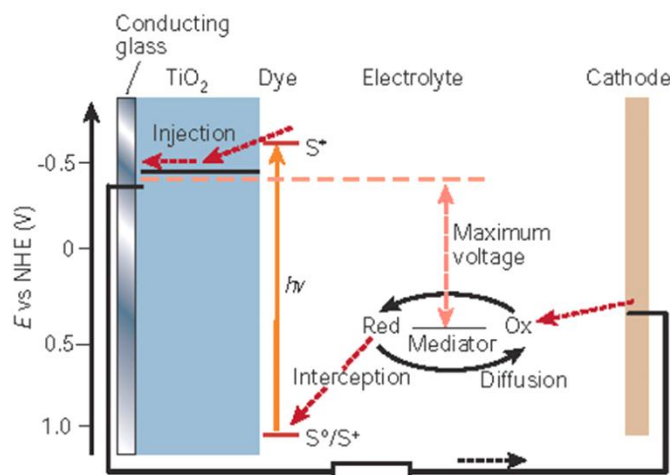


Figure 2.7 Schematic of operation of the DSSC (Gratzel, 2001).

In either model, the e^- may be localized near the surface or in the bulk, and during their transit the e^- may partially loss by transfer across the solid/liquid interface to I_3^- . The efficiency of collecting the photoexcited e^- , which is determined by competition between electron transport to the anode and electron transfer to I_3^- in the electrolyte, is critical to enhance the device performance (Jennings *et al.*, 2008).

2.3 TiO_2 nanotube arrays

Particulate TiO_2 film has been used since the discovery of PEC (Fujishima and Honda, 1972) and DSSC (O'regan and Gratzel, 1991). However, random pathway of e^- transport in particulate TiO_2 film leads to the recombination through trapping/detrapping of photogenerated e^-/h^+ (Kudo and Miseki, 2008; Lei *et al.*, 2010; Mohamed and Rohani, 2011). 1D nanostructures have triggered enormous effort in physics, chemistry, and materials science of nanomaterials. TiO_2 with well-aligned nanotubular structure provides unique electronic properties, such as high e^- mobility, low quantum confinement effects, high specific surface area, excellent ability to absorb $h\nu$, and high mechanical strength (Mohapatra *et al.*, 2007; Baker and Kamat, 2009; Roy *et al.*, 2011). Furthermore, vectorial charge transport in well-aligned tubular structure greatly contributes to better photoelectrochemical properties and photocatalytic efficiency as compared to randomly-oriented nanoparticles (Baker and Kamat, 2009; Mohamed and Rohani, 2011). These advantages render TiO_2 nanotube arrays as promising candidate for various applications; pollutant decomposition (Chen *et al.*, 2009; Sangpour *et al.*, 2010), PEC (Park *et al.*, 2006; Mohapatra *et al.*, 2007; Palmas *et al.*, 2010) and DSSC (Jennings *et al.*, 2008; Lei *et al.*, 2010; Premalal *et al.*, 2012; Chang *et al.*, 2012). Hence, the correlation of structural

morphologies and performance of TiO₂ nanotube arrays is elaborated in subsequent section.

2.3.1 Anodic growth of self-organized TiO₂ nanotube arrays

TiO₂ nanotubes have been fabricated through various methods, such as sol-gel (Maiyalagan *et al.*, 2006; Kang *et al.*, 2009), hydrothermal (Yu *et al.*, 2008; Sreekantan and Lai, 2010), chemical vapor deposition (Hsieh *et al.*, 2010) and electrochemical anodization (Gong *et al.*, 2001; Macak and Schmuki, 2006; Sohrab and Ahmed, 2009). However, electrochemical anodization has been recognized as an efficient and facile approach to produce integrative, vertically-oriented highly-ordered nanotube arrays with controllable structural morphologies without any additional process (Roy *et al.*, 2011; Mohamed and Rohani, 2011).

Electrochemical anodization can be defined as well-desired electrochemical growth of an oxide film on a metal substrate by polarizing the metal anodically in an electrochemical cell. Anodization can be conducted by *i*) applying a constant potential difference between anode and cathode; potentiostatic mode, *ii*) by imposing constant current; galvanostatic mode, or *iii*) by sweeping the anode potential at given rate; potentiodynamic mode (Pasquale *et al.*, 2006; Kaneco *et al.*, 2007; Miraghaei *et al.*, 2011; Vanhumbecck and Proost, 2011). Potentiostatic anodization has widely been used to grow oxide films due to its extreme simplicity (Mohapatra *et al.*, 2007; Baker and Kamat, 2009; Roy *et al.*, 2011). Zwilling *et al.* (1999) first demonstrated the formation of self-organized porous TiO₂ via potentiostatic anodization of Ti in chromic acid (H₂CrO₄) containing hydrofluoric acid (HF). The obtained tube-like structure was not highly organized, and it showed considerable sidewall

inhomogeneity. From this origin, the presence of fluoride ions (F^-) in electrolyte has been recognized as an essential in anodic growth self-organized oxide structures. The anodic growth of self-organized structure mainly involves with electrochemical oxidation and chemical dissolution. A compact oxide layer initially forms on the metal surface; M involving metal ion formation; M^{z+} (Reaction 2.9), and consequently reacted with oxide ion (O^{2-}) and/or hydroxyl ions (OH^-) via field-assisted oxidation –refer to Reaction 2.10 – 2.11 (Shankar *et al.*, 2007; Roy *et al.*, 2011). The oxide formation mechanism on a metal is illustrated in Figure 2.8a.



In principle, four different morphologies, including compact structure, random porous structure, oriented porous structure and oriented tubular structure can be obtained by anodization (Figure 2.8b). Chemical dissolution plays an important role to determine the structural morphologies of anodic oxide. After the formation of an initial oxide layer, the O^{2-} and/or OH^- ions migrate through the oxide layer reaching the metal/oxide interface and then react with the metal. High electric field at initial oxide layer dominates the polarization of the M^{z+} –O bond (Mor *et al.*, 2006; Zhang *et al.*, 2010). The M^{z+} consequently migrates from the metal at the metal/oxide interface and moves outwards the oxide/electrolyte interface.

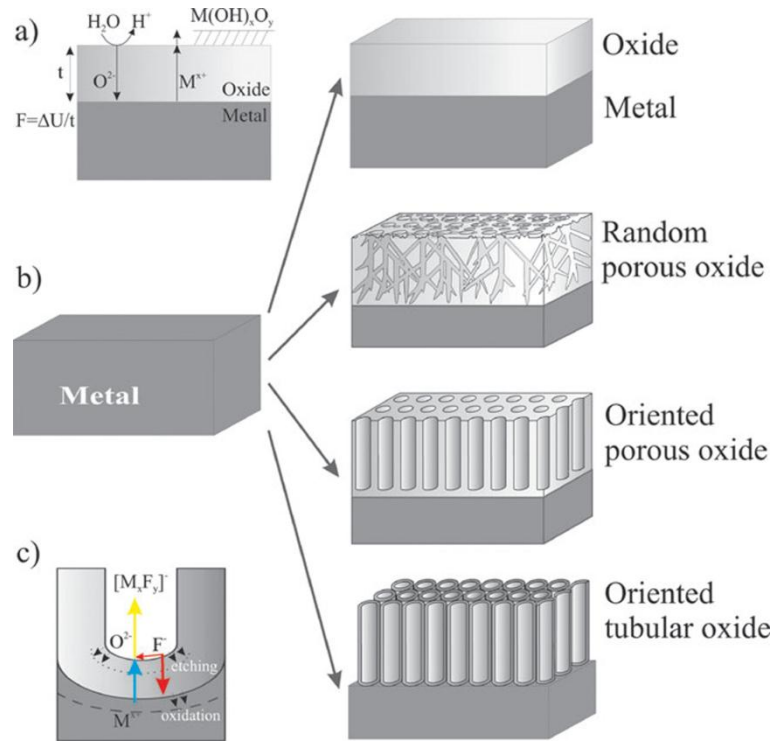
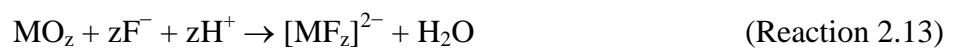


Figure 2.8 (a) Oxide formation mechanism on a metal. (b) Morphologies which can be obtained by anodization of Ti metal –a compact oxide film, a disordered nanoporous layer, a self-ordered nanoporous or a self-ordered nanotube layer. (c) Nanotube formation mechanism (Ghicov and Schumuki, 2009).

Besides, the presence of F^- in electrolyte strongly affects the anodization process, as F^- subsequently forms soluble complex $[MF_z]^{2-}$ species (Figure 2.8c). On the other hand, complexation occurs with M^{z+} ion migrated from the oxide/electrolyte interface (Reaction 2.12), and consequently attaches to the formed oxide –refer to Reaction 2.13 (Ghicov and Schumuki, 2009; Roy *et al.*, 2011).



Gong *et al.* (2001) investigated the significance of electrochemical dissolution and chemical dissolution in aqueous electrolyte on the anodic growth of TiO_2 oxide by

varying applied potential over the range of 5 – 20 V, and HF concentration of 0.5 – 3.5 wt%. Porous and particulate structure was formed in aqueous electrolyte containing 0.5 wt% HF under applied potential lower than 10 V. Self-organized tubular structure was successfully formed at 10 – 20 V. It was noticeable that an appropriate applied potential for the formation of TiO₂ nanotube arrays is disproportional to the HF concentration. These reveal the essential of anodization parameters on the formation and structural morphologies of TiO₂ nanotube arrays.

2.3.2 Factors affecting geometry and composition

The anodic growth of self-organized tubular structure is well known as the equilibrium reaction between electrochemical oxidation at the metal/electrolyte interface and chemical dissolution at the oxide/electrolyte interface (Macak *et al.*, 2005; Shankar *et al.*, 2007). The structural characteristics of the nanotube arrays can be controlled through various synthesis parameters, including applied potential (Cai *et al.*, 2005; Paulose *et al.*, 2007; Lockman *et al.*, 2010), anodization time (Cai *et al.*, 2005; Wan *et al.*, 2009; Antony *et al.*, 2012), electrolyte type and chemical composition (Macak *et al.*, 2005; Ruan *et al.*, 2005; Shankar *et al.*, 2007). Therefore, this section provides a comprehensive review on the influence of aforementioned parameters on the formation of TiO₂ nanotube arrays.

2.3.2.1 Nanotube arrays synthesis using aqueous electrolytes

Gong and co-workers (2001) first obtained self-organized, highly-uniform TiO₂ nanotube arrays by anodizing Ti in aqueous electrolyte containing 0.5 wt% HF under applied potential of 10 – 20 V. The pore size increased with increasing applied potential while the nanotube length was dependent on the anodization time.

However, the length of nanotubes was limited to a maximum of ~500 nm, due to the restriction imposed by high chemical dissolution of formed oxide by strong acidity of HF aqueous electrolyte, *c.a.*, $\text{pH} < 2$ (Cai *et al.*, 2005; Mohamed and Rohani, 2011). The chemical dissolution of the formed oxide is determined by the F^- concentration and the pH value of the solution –refer to Reaction 2.13 (Cai *et al.*, 2005). Large number of F^- and H^+ ions in HF aqueous electrolyte dominates high chemical dissolution and thus hinders the equilibrium growth of the nanotube arrays (Macak *et al.*, 2005). Beranek *et al.* (2003) found that the incorporation of low concentration of HF aqueous electrolyte with acetic acid (H_2SO_4) addition could reduce the chemical dissolution, and thus allows the formation of porous TiO_2 with improved structural morphologies. This basis was later used to obtain TiO_2 nanotube arrays with well-defined tubular structure over applied potential range of 10 V to 25 V (Cai *et al.*, 2005). The nanotube length and pore diameter increased linearly with increasing applied potential. In summary, the structural morphologies of anodic growth oxides can be controlled by the acidity of electrolyte (Sreekantan *et al.*, 2009).

Macak *et al.* (2005) investigated the influence of the electrolyte acidity on the growth of nanotube arrays using HF, potassium fluoride (KF) and sodium fluoride (NaF) as F^- sources. TiO_2 nanotube arrays with ~280 nm long and ~40 nm pore diameter were formed in strong acidity ($\text{pH} < 1$) HF aqueous electrolyte after 2 h of anodization at 10 V. The increase in the pH value of electrolyte to 1.3 and 2.8 by using KF and NaF instead of HF resulted in the formation of TiO_2 nanotube arrays with the nanotube length of ~320 nm and 590 nm, respectively. TiO_2 nanotube arrays with a maximum length of 1.5 μm were achieved at 25 V (Figure 2.9a – c). Moreover, the nanotube length is proportional to the anodization time, and thus